AIAA SciTech Forum
8-12 January 2024, Orlando, FL
AIAA SCITECH 2024 Forum

10.2514/6.2024-1774

Wind Tunnel Installation Effects on the Base Flow for a High-Speed Exhaust System

Spyros Tsentis*, Ioannis Goulos†, Simon Prince‡ and Vassilios Pachidis§
Cranfield University, Cranfield, United Kingdom, MK43 0AL

Vladeta Zmijanovic¶
Reaction Engines Ltd., Oxford, United Kingdom, OX14 3DB

Josè Saavedra‖
Rolls-Royce Plc., Bristol, United Kingdom, BS34 7QE

It is envisaged that future propulsion concepts will enable high-speed flight and improve space access. However, their aerodynamic behavior is not yet well understood, especially at the base where severe flow separation occurs, requiring further analyses using both numerical and experimental techniques. This paper presents a numerical investigation of the wind tunnel installation effects on a representative, sub-scale, high-speed exhaust system. The analysis facilitates an ongoing design of experiments and de-risking activity. The apparatus features a truncated, ideal-contoured nozzle and an axially symmetric cavity region embedded at the base. The viable design space owing to high blockage is identified in terms of maximum approach Mach number. A systematic jet vectoring effect is observed in all cases examined. The origins of this effect are investigated and attributed solely to the pressure distribution asymmetry caused by the existence of the wing-pylon. Additionally, local flow similarity at the base of the tunnel-installed model with respect to unconstrained flow is investigated and presented, along with a proposed methodology to establish comparability. This analysis is of increased practical importance, due to the size range of most closed transonic tunnels found in academic research facilities. Results show that the pressure distribution at pre-choking tunnel conditions agrees within less than 1.5% and 0.1% for the base and cavity wall surfaces, respectively. At post-choking tunnel operation, the base pressure distribution of the model exhibits increased deviations in the azimuthal direction of up to 7.5%. The base pressure distribution in the corresponding unconstrained flow case falls within the observed pressure range of the tunnel-installed model, while the pressure distribution along the cavity wall agrees within less 1%. The findings of this study suggest that a jet vectoring effect could potentially manifest to wingtip mounted nacelles, usually incorporated in future, high-speed vehicles. Finally, it is demonstrated, that local flow similarity exists at the base with respect to unbounded flow, even for post-choking tunnel conditions, which is critical in base flows and base drag reduction analyses.

I. Nomenclature

C_D	=	nozzle discharge coefficient
$C_{V,s}$	=	nozzle standard velocity coefficient
F_G	=	gauge stream force [N]
L	=	total length of the model [m]
M_a	=	wind-tunnel approach Mach number

*Ph.D. Researcher, Centre for Propulsion and Thermal Power Engineering, Cranfield University, spyros.tsentis@cranfield.ac.uk
†Senior Lecturer in Propulsion Aerodynamics and Performance Engineering, Centre for Propulsion and Thermal Power Engineering, Cranfield University, i.goulos@cranfield.ac.uk
‡Professor of Aerodynamics, Centre for Aeronautics, Cranfield University, simon.prince@cranfield.ac.uk
§Professor and Head of Centre for Propulsion and Thermal Power Engineering, Cranfield University, v.pachidis@cranfield.ac.uk
¶Senior Aerothermal Engineer, Reaction Engines Ltd., vladeta.zmijanovic@polytechnique.edu
‖Aerothermal Systems Engineer, Rolls-Royce Plc., jose.saavedra@rolls-royce.com

M^b_{eff} = effective Mach number at the base
M_∞ = free-stream Mach number for unbounded flow
p = static pressure [Pa]
T = static temperature [K]
P_0 = total pressure [Pa]
T_0 = total temperature [K]
y^+ = non-dimensional wall distance
θ = fluid force in thrust domain [N]
ϕ = fluid force in drag domain [N]
τ_w = viscous shear stress on the wall [Pa]

II. Introduction

A. Background

High-speed propulsion concepts have been studied for many years to enable supersonic flight as well as easier space access. Such concepts are usually related to launch vehicles and rocket-based transportation systems. However, air-breathing propulsion has also been considered for such concepts [1, 2], often utilizing systems which feature no rotating components such as Ramjets [3] and Scramjets [4]. Due to their operating principle being based on ram air compression, Ramjets and Scramjets cannot generate static thrust. This has led to the development of more advanced, combined cycle concepts, comprising Turbine-based [5] and Rocket-based [6] combined cycles (TBCC and RBCC respectively), among others.

Pre-cooled, combined cycle engines is another technology that has received attention for future sustainable, high-speed propulsion. This air-breathing concept incorporates a heat-exchanger to cool down the incoming air prior to compression [1]. This facilitates the extended operational range of the downstream turbomachinery and thus, allows the engine to operate at higher Mach numbers, in contrast with most contemporary air-breathing systems. Several concepts based on this principle have been studied over the years [7] and have been found to exhibit significantly improved efficiency, especially over chemical rocket engines in the case of space access [8, 9]. While the performance advantage is well-established from a thermodynamic point of view, the aerodynamic behavior of these concepts is not yet well understood. Such concepts often feature convergent-divergent (C-D) exhaust nozzles at the base to reach the high speeds required for their designed missions. Due to their implementation, the nozzle is usually embedded at the base. This poses a major difference, in terms of canonical base flow physics, compared to contemporary launch vehicles where the propulsive nozzle juts out of the base. Additionally, cavity regions are often employed in these concepts to facilitate the overall design of the system, and could potentially further modify their aerodynamic behavior. Consequently, further analysis is required for such concepts to understand the salient flow features at the base.

B. Base flow characteristics

The flow characteristics at the base region of launch vehicles and propulsive configurations in general, have a critical effect on the overall aerodynamic performance of the system. The distribution of pressure at the base, ergo the base drag, is highly dependent on the geometrical aspects of the vehicle's base, on the free stream flow conditions, on whether the engine is on or off, as well as on the operating state of the propulsive nozzle (i.e., over- or under-expansion for a powered-on configuration). These phenomena have been widely investigated over the years utilising both experimental and numerical activities. Most of the research effort in the public domain is focused on axisymmetric configurations incorporating blunt-based bodies [10–12] and backward facing steps (BFS) [13, 14], owing to the axisymmetric topology usually found in space launchers. However, studies on planar, powered-on configurations featuring a dual-bell nozzle at the base can also be found [15].

Saile et al. [16] carried out experiments employing a powered BFS configuration aiming at the analysis of the buffeting effect at the base region of space launchers, similar to the European launcher Ariane 5, in the subsonic regime of the mission ($0.5 < M_\infty < 0.9$). A large-scale, rotating vortex was identified in the separated base region which caused high turbulence intensity levels. At M_∞=0.8, an exceptionally excited area was shown to develop which is in agreement with the critical situation in terms of side loads during the ascent of the launcher as reported by Schwane [17]. Additionally, the effect of the nozzle extension length was investigated later on [18], and was found to affect the base flow unsteadiness, with the most unfavorable geometry reported at relative nozzle lengths of L/D=0.9, where D corresponds

to the diameter of the main cylindrical body of the BFS configuration and L to the nozzle extension length. Statnikov et al. [19] performed numerical computations employing a hybrid, zonal Reynolds-averaged Navier-Stokes/Large Eddy Simulation (RANS/LES) approach, to examine the wake of a cylindrical BFS, featuring an under-expanded, truncated, ideal-contoured (TIC) nozzle at conditions of $M_\infty = 6$. At a nozzle pressure ratio of 100, the displacement effect of the plume and the shear layer, formed a subsonic cavity at the step extension which amplified the shear layer instability. Paciorri et al. [14] investigated the base flow with and without a cold propulsive jet for a generic space launcher topology, utilising a BFS configuration in the range $0.18 < M_\infty < 0.43$. A decrease in the base pressure, therefore increase in base drag, for the jet-on case was the result of the aspiration effect [20]. However, this effect was mitigated by extending the nozzle exit section further away from the base, which demonstrates the fundamental difference of base-embedded nozzles compared to configurations where the nozzle (or nozzles) juts out of the base.

Even though axisymmetric BFS configurations have been extensively employed in past numerical and experimental studies owing to their representative nature and reduced complexity, results on more detailed base configurations of launchers have also been reported. Meliga and Reijasse [21] investigated the effect of side boosters on the base flow topology of such axisymmetric BFS geometries. They reported a notable 50% decrease in the base pressure coefficient at the presence of the boosters compared to the BFS configuration alone. Furthermore, description of numerical and experimental approaches for the investigation of the European launchers Ariane 5 and Vega as well as results on their side loads, can be found in the study of Schwane [17]. The BFS geometry, typically employed in the vast majority of previous base flow studies, is strongly associated with the design of contemporary space launch vehicles, where the nozzle juts out of the base. This effect can be simplified and represented, in terms of canonical flow physics, with an axisymmetric BFS configuration. However, several advanced, combined cycle propulsion concepts, as the ones mentioned earlier, feature a base-embedded nozzle topology, where the nozzle exit is co-planar with the engine's base. This affects the corresponding flow physics at the base and near-wake regions [14], and therefore a BFS configuration can no longer be considered as representative. Consequently, further analysis is required for these concepts, especially in the vicinity of their base and exhaust system.

Additionally, these concepts usually employ base-embedded cavities to facilitate their overall design and in-flight operation, which could further modify their aerodynamic behavior compared to contemporary rocket-based systems. Cavity effects could potentially arise from the necessity for nozzle gimballing capabilities, thermal protection for critical engine's components and/or co-planar, separate-jet exhausts where the secondary exhaust system is inactive. While there have been many studies in the open literature on base geometry modifications with base cavities [22, 23], these studies mainly focus at quantifying the effectiveness of cavities as a passive base drag reduction technique [24–26]. Analyses on exhaust systems, where base-embedded cavities are employed as an integrated design aspect of the system, necessary for successful operation, have not been previously reported in the public domain. However, the significance of such cavities has been demonstrated in previous work by the authors [27], where the existence of the cavity alone, transitioned the nozzle operation into the under-expanded condition at $M_\infty = 1.2$. This led to a notable increase of approximately 12% in the drag coefficient with respect to an identical, non-cavity configuration, as a result of higher base drag. Therefore, it is clear that further investigation on the base flow of such novel concepts is required, making use of both numerical and experimental techniques.

C. Limitations in experimental testing

As discussed previously, a critical condition for launch vehicles, in terms of increased side loads, occurs during transonic flight [16, 17]. It is well-established that transonic flow is highly unsteady and challenging to predict numerically. Base flow analysis is often facilitated through experimental approaches and wind tunnel testing. Such techniques provide important insights into the underlying flow physics at the base as well as useful data sets that can be utilized to perform a validation activity against numerical results [28]. However, there are often practical limitations involved in experimental testing of such configurations, including the size of the test section of most closed transonic wind tunnels found in academia, which tend to be at the size range of $\sqrt{A}$=0.1-0.25 m as reported by Greenwell [29], where A denotes the test section cross-sectional area. This, along with the relatively large size of the investigated model, usually imposed by instrumentation and necessity for high Reynolds numbers, could lead to large blockage ratios (BRs) and therefore, increased wind tunnel integration effects. The required size of the model and support can increase notably in the case of powered-on base flows, owing to the requirement of accommodating a secondary flow. Wind tunnel integration effects include flow interaction phenomena caused by the presence of the tunnel walls (especially if they feature no perforation) and the mounting device of the model [30]. Additionally, at high enough BRs and/or approach Mach numbers, tunnel choking could ultimately occur. These effects can notably modify the flow-field in terms of

pressure distribution around the model and hence, negatively affect flow similarity with respect to unbounded flow conditions. For a choked tunnel in specific, flow similarity is usually rendered invalid as the flow-field in the free-stream case differs significantly from the one observed in the wind tunnel [31]. Even though there have been successful efforts to intentionally choke the flow in a wind tunnel to simulate Mach 1 conditions around simplified bodies such as a double wedge airfoil [32], tunnel choking is typically undesirable and limits the design space where valid data can be acquired [31].

Wind tunnel integration effects have been traditionally studied by experimenters and theoreticians over the years with the main focus of identifying the impact of tunnel walls and blockage on the aerodynamic characteristics of the investigated model. Several correction methodologies have been developed to account for such effects and are widely used on wind tunnel data, especially when integral metrics such as lift and drag coefficients are of primary interest. A comprehensive summary of correction methodologies for several types of wind tunnels can be found in [33, 34] as reported by the Advisory Group for Aerospace Research and Development (AGARD). Whilst essential, application of corrections to experimental data to account for wall interference and blockage effects gets more intricate as the geometry of the model gets more complex. Additionally, correcting the experimental data to produce unbounded-flow equivalent results is not always the main objective of an experimental campaign. This is especially true in academic facilities where research on relatively new concepts is being conducted and hence, understanding of dominant flow features usually has priority over acquiring data that can be corrected for free-stream conditions. A typical example of this scenario, in the context of base flows, is the investigation of base geometry modifications to assess their base drag reduction capabilities [23]. In this case, correction of the results becomes less important as the main objective is to examine the potential of a concept as a base drag reduction technique, from a flow physics perspective. However, even at this case, severe tunnel integration effects, as those previously mentioned, might significantly affect the flow at the base and therefore, lead to erroneous or misleading results with respect to unbounded flow conditions. The answer to that question becomes particularly important in the case of university facilities, where transonic closed wind tunnels sit at the lower end of the size range compared to their industrial counterparts [29]. Studies addressing this research question either qualitatively or quantitatively, regarding the potential impact of wind tunnel integration effects on the local base flow characteristics, have not been reported in the public domain.

D. Scope of present work

This paper presents a numerical investigation on the wind tunnel integration effects for a sub-scale, high-speed exhaust system, featuring a cold flow, TIC nozzle along with an axisymmetric cavity region embedded at the base. The examined configuration is representative of future advanced propulsion concepts, usually incorporating base-embedded, C-D nozzles and axisymmetric cavities. Three-dimensional, Reynolds-averaged Navier-Stokes computations are employed to analyse the flow behavior of the tunnel-installed model. It should be stressed, that RANS-based computations pose well-known limitations in identifying unsteady phenomena, especially for largely separated base flows. However, within the context of this work, this approach serves as a computationally efficient, de-risking activity to facilitate the overall design of experiments of an ongoing experimental campaign through the characterisation of salient flow features in an average sense.

The effect of tunnel pressure ratio (TPR) and nozzle pressure ratio (NPR) on the flow characteristics, approach Mach number of the tunnel M_a, as well as Reynolds number Re, is evaluated in the range of $1.28 < TPR < 1.79$ and $5 < NPR < 20$ respectively. Three-dimensionality effects that manifest in the tunnel-installed model and the impact of blockage ratio are identified, along with the region of the examined design space which is viable for insightful experimental measurements. A direct comparison of the tunnel-installed model to an identical configuration where the effect of the tunnel walls has been totally removed, facilitates the characterisation of the pylon's impact on the exhaust. Practical limitations that are posed upon the experimental activities are demonstrated along with their origins, which could apply in any similar campaign involving powered-on, base flow simulations and experiments. Additionally, the question whether local flow similarity at the base with respect to unconstrained flow can be achieved, is addressed, along with a systematic methodology which allows the free-stream and tunnel-installed cases to be compared. To the authors' best knowledge, the impact of wind tunnel integration on the global and local flow characteristics of high-speed exhaust systems, featuring a base-embedded, C-D nozzle and cavity, have not been reported in previous studies.

III. Methodology

A. Experimental details and investigated configuration

The ongoing campaign aims to generate experimental data that will serve to investigate the base flow unsteadiness, cavity effects and overall behavior of future representative high-speed exhaust systems as well as to facilitate a systematic numerical validation activity. The experiments are designed to be performed in the closed-circuit, ejector-driven transonic wind tunnel (TSWT) at the Defence Academy of the United Kingdom. The facility has a working cross-section of Hxh = 228x207 mm and features solid walls without perforation. The flow conditions in the tunnel are controlled through the pressure regulation of the ejector system, which is located downstream of the test section. This pressure is denoted as p_{out} in the following study. The total pressure of the flow approaching the model $P_{0,t}$ is approximately atmospheric. Therefore, the tunnel pressure ratio, defined as TPR=($P_{0,t}/p_{out}$) herein, is regulated by altering the outlet pressure of the wind tunnel. Figure 1 shows a schematic of the model and tunnel configuration that is numerically investigated in this study in both xz and yz planes. The model comprises a nacelle surface which is formed by the main cylindrical body and an ogive-shaped nose. It is attached to the bottom tunnel wall through the pylon which has a NACA 0024 profile cross-section. The maximum pylon thickness and length, non-dimensionalized over the model's diameter D, are approximately 0.46 and 1.74, respectively. The relatively large size of the pylon is driven by the thickness required to accommodate the corresponding mass flow conditions in the nozzle as dictated through the NPR, from an experimental point of view. The dimensions of the tunnel cross-section relative to the model's diameter are approximately equal to H/D = 2.85 and h/D = 2.6, where H and h are defined in Fig. 1.

The model features a high-speed, TIC nozzle embedded at the base. The wall contour of the nozzle in the divergent section is designed using the axisymmetric Method of Characteristics (MoC) [35] to obtain a shock-less flow expansion. Sauer's small perturbation technique [36] is employed at the throat region to approximate the near critical flow conditions and used as an initial-value line for the MoC procedure in the downstream supersonic flow. The resulting ideal nozzle is then truncated at an angle of 7.6 degrees, which corresponds to a design exit Mach number of approximately 3.4 and a design nozzle pressure ratio of NPR_d=59. The gray shaded area in the yz plane view of the model in Fig. 1 corresponds to the maximum thickness of the pylon. It is clear from Fig. 1 that the blockage ratio (BR), defined as the area ratio of the largest cross-section of the model and pylon over that of the test section, is large and approximately equal to (A_{model}/A_{tunnel})=0.165, which is slightly higher than the maximum one usually recommended of 0.16 [30]. Further reduction of the model dimensions to reduce the blockage ratio is very challenging, owing to the nozzle and cavity flows which are critical in this campaign as well as for instrumentation reasons. Therefore, it is expected that the tunnel walls, as well as the pylon, will have an effect on the base flow of interest, which is essential to be understood before any

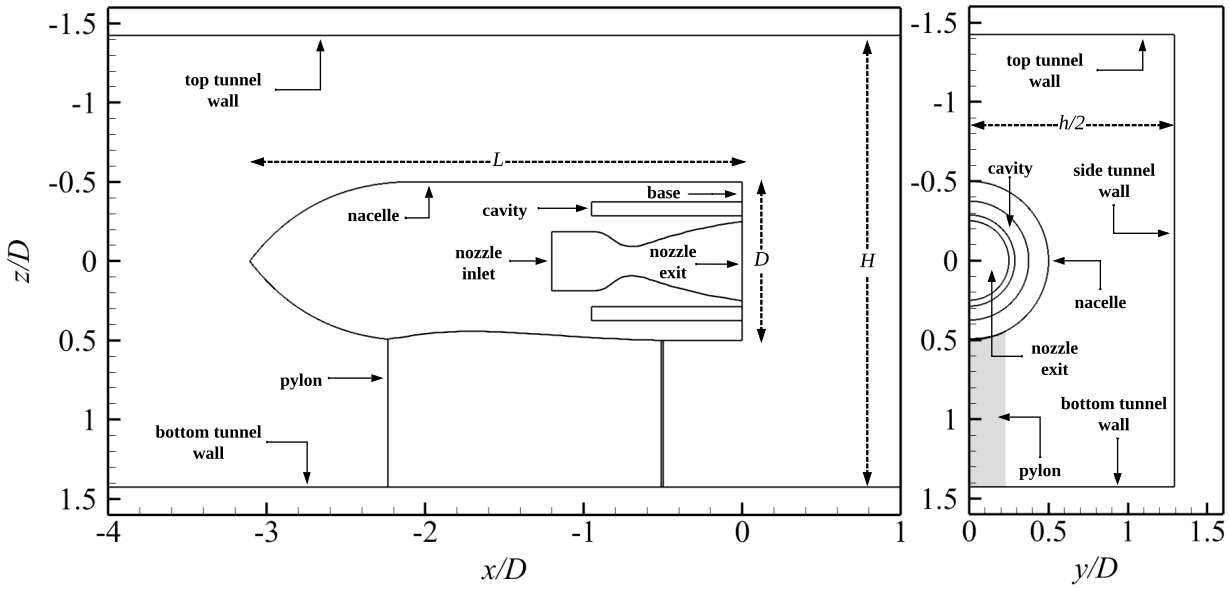

Fig. 1 Configuration of the tunnel and exhaust system shown in the xz (left) and yz (right) planes

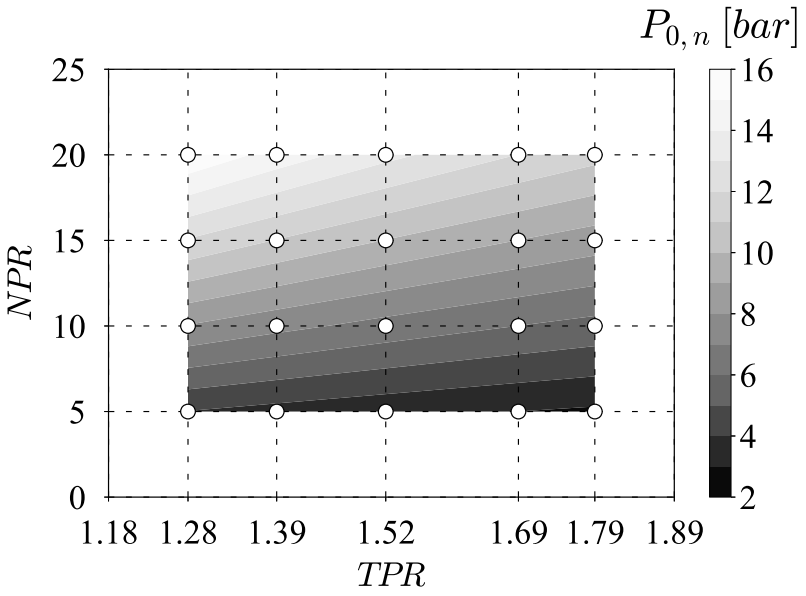

Fig. 2 Variation of $P_{0,n}$ within the examined design space; White circles denote the test cases

experimental activities initiate.

It is critical to investigate the behavior of the tunnel-installed, sub-scale model in terms of the variables that will form the design space of the experimental activities in order to establish consistency. Figure 2 shows the examined design space in terms of TPR and NPR that is investigated numerically in this study. The exact flow conditions of the test cases are indicated with white circles. Owing to the large blockage ratio, it is expected that for a number of the examined cases, the conditions at the tunnel inlet will be heavily dependent on the flow conditions in the vicinity of the model. For this reason, and to avoid ambiguous definition in the design variables, within the context of this work NPR is defined as the ratio between the inlet total pressure of the nozzle $P_{0,n}$, over the outlet static pressure of the tunnel p_{out}. Different values of TPR are examined for fixed $NPRs$. As depicted in Fig. 2, this is achieved through the regulation of $P_{0,n}$ and serves to establish orthogonality between NPR and TPR, which would be otherwise contaminated if constant values of $P_{0,n}$ where to be used. A combination of five different tunnel pressure ratios (TPR=1.28, 1.39, 1.52, 1.69, 1.79) and four nozzle pressure ratios (NPR=5, 10, 15, 20) are examined, producing a total number of 20 investigated scenarios for the tunnel-installed model (Fig. 2).

B. Performance accounting methodology

In order to properly evaluate the aerodynamic performance of the exhaust system under investigation as well as the effect of the tunnel walls and pylon, a performance accounting system must be first established to ensure consistency. Figure 3 illustrates the thrust and drag accounting methodology as employed in this study, which is based on a well-established thrust-drag book-keeping system [37]. A near-field approach is selected to facilitate the direct evaluation of the constituent elements of the total forces. The aerodynamic forces exerted on the wall surfaces of the model and pylon by the fluid flow that reside within the drag and thrust domains are denoted by the symbols ϕ and θ, respectively. These aerodynamic forces are obtained through direct numerical integration of the gauge static pressure and shear-stress terms along the wall viscous surfaces, as described in Eq. (1). The gauge stream force F_G as well as the mass flow rate at the nozzle inlet and exit are evaluated through numerical integration at the corresponding boundaries (Eq. (2)).

$$\theta,\ \phi = \iint_S (p - p_\infty) \sin a \, dS + \iint_S t_w \cos a \, dS \tag{1}$$

$$F_G^x = \iint_{Area} \rho u_x^2 dA + \iint_{Area} (p - p_\infty) dA \tag{2}$$

In Eq. (1), p and τ_w refer to the local static pressure and shear stress respectively, p_∞ refers to the ambient static pressure, here taken at the tunnel outlet, a is the local surface angle measured from the axial direction and dS is the elemental surface area. In Eq. (2), ρ is the density, u_x is the axial velocity component and dA is the elemental surface area of the corresponding boundary. In order to assess the aerodynamic performance of the exhaust nozzle, the standard velocity coefficient $C_{V,s}$ is used, which represents the ratio of the calculated standard gross thrust $F_{G,s}$, over the ideal thrust (Eq. (3)). The latter, corresponds to the thrust that the system would produce under isentropic, fully-expanded flow to the ambient static pressure. The standard gross thrust is the gauge stream force at the exit of the nozzle and is described in Eq. (4) based on control volume theory. The ideal exit velocity term, appearing in the denominator of Eq. (3), corresponds to the ideal jet exit velocity that would be reached under isentropic expansion to the ambient static pressure and is defined as shown in Eq. (5).

$$C_{V,s} = \frac{F_{G,s}}{\dot{m}_{actual}\, V_{ideal}} \tag{3}$$

$$F_{G,s} = F_{G,inlet} - \theta_{nozzle} \tag{4}$$

$$V_{ideal} = \sqrt{\frac{2\gamma R T_0}{(\gamma - 1)} \left(1 - \left(\frac{1}{NPR}\right)^{\frac{\gamma-1}{\gamma}}\right)} \tag{5}$$

where NPR is the nozzle pressure ratio as defined previously, R is the gas constant, γ is the ratio of specific heats and T_0 is the total temperature at the nozzle inlet. Due to the investigated cases in this study, the nozzle discharge coefficient C_D is not examined, since the nozzle is expected to operate under choked conditions. The summation of the aerodynamic forces that are exerted by the fluid flow on the surfaces and reside within the drag domain, as defined previously (Fig. 3), constitute the total modified drag force [37], and is expressed as follows:

$$D^* = \phi_{nacelle} + \phi_{base} + \phi_{cavity} + \phi_{pylon} \tag{6}$$

The gross propulsive force GPF, represents the overall aerodynamic force component in the free-stream flow direction, which is produced by the exhaust system and is obtained as described by Eq. (7). The GPF allows the overall aerodynamic performance to take into account the regions of separated flow within the nozzle under over-expanded conditions.

$$GPF = F_{G,s} - D^* \tag{7}$$

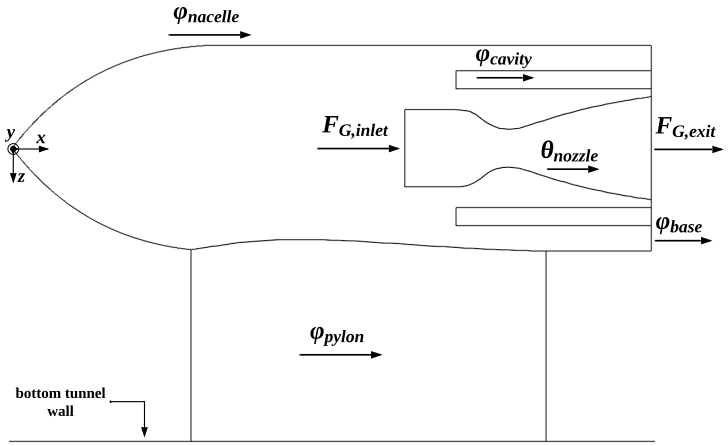

Fig. 3 Thrust and drag accounting system for the tunnel-installed model

C. Computational methods and approach

A half-tunnel approach is employed in this study to construct the computational domain, making use of the xz symmetry plane and thus, drastically reducing the associated computational cost and increasing efficiency (Fig. 4). The domain extends downstream of the base at a distance equal to 10 times the total length of the model L. The conditions at the tunnel inlet are modelled by applying a pressure inlet boundary condition (BC) on the corresponding surface, with total pressure and temperature as the prescribed values. At the outlet of the computational domain, a pressure outlet BC is applied, imposing the static pressure value p_{out}. The total pressure and temperature at the nozzle inlet are defined by applying a pressure inlet BC. The light pink shaded area of Fig. 4 corresponds to the symmetry plane xz and therefore, a symmetry BC is applied. All surfaces of the model, pylon and tunnel, are modelled as viscous no-slip and adiabatic walls. A hybrid meshing approach is employed in this study [38]. Figure 5 depicts a close-up view of the derived surface mesh at the base and near-wake regions as well as on the cavity and nozzle. The hybrid approach employs 35 prism layers near the wall surfaces of the model, pylon and tunnel to allow for proper boundary layer resolution. The resulting y^+ is below 1 for all wall-adjacent nodes. The remainder of the domain is discretized in an unstructured manner, employing polyhedral elements. This type of elements is usually more efficient in terms of cell count compared to tetrahedrons. Additionally, polyhedral elements have been considered in a broad range of aerodynamic flow simulations, including helicopters [39] and buildings [40] among other, and have been found to exhibit similar levels of accuracy as that of more conventional element topologies (e.g., tetrahedrons). Unstructured mesh refinement regions are employed to gradually migrate from the undisturbed flow conditions at the tunnel inlet to the after-body, base and near-wake regions of the domain, where better resolution is desired (Fig. 5). A cell growth ratio of 1.2 has been maintained throughout the grid generation process. Additionally, the finest grid resolution region extends downstream of the base at a length equal to 12.5 nozzle exit radii.

A grid convergence study was conducted to assess the discretization error, based on the generalized Richardson Extrapolation procedure [41] and using the second order Grid Convergence Index (GCI) [42]. The grid refinement process was done in a systematic manner by uniformly refining the surface and volume elements based on the local spatial discretization of that region of the mesh (Fig. 5), while additional prism layers were added to ensure that consistency with the unstructured grid of the domain is maintained. Therefore, grids comprising 3, 13.7 and 44 million cells were used, providing a grid refinement factor higher than 1.3 as suggested in [42]. A detailed summary of the results of the grid convergence analysis is shown in Table 1. The investigation of the standard velocity coefficient $C_{V,s}$, allows to evaluate the nozzle operation and efficiency alone (Eq. (3)), while GPF constitutes an overall metric since it

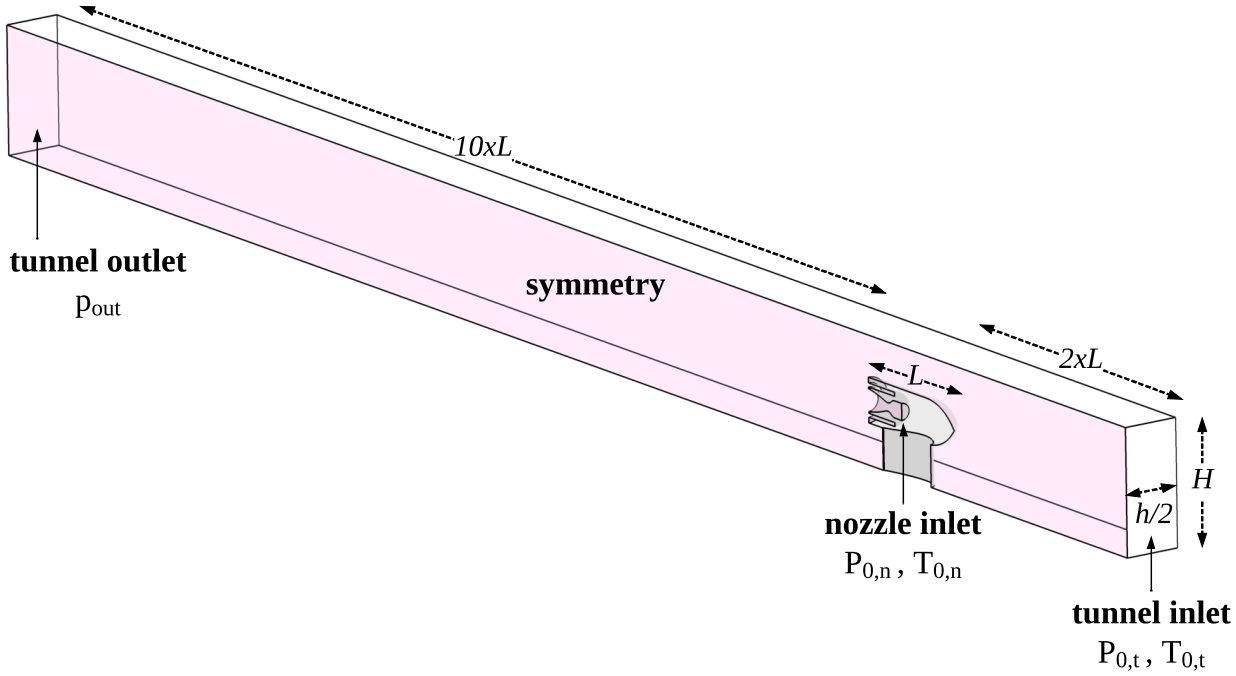

Fig. 4 Computational domain and boundary conditions

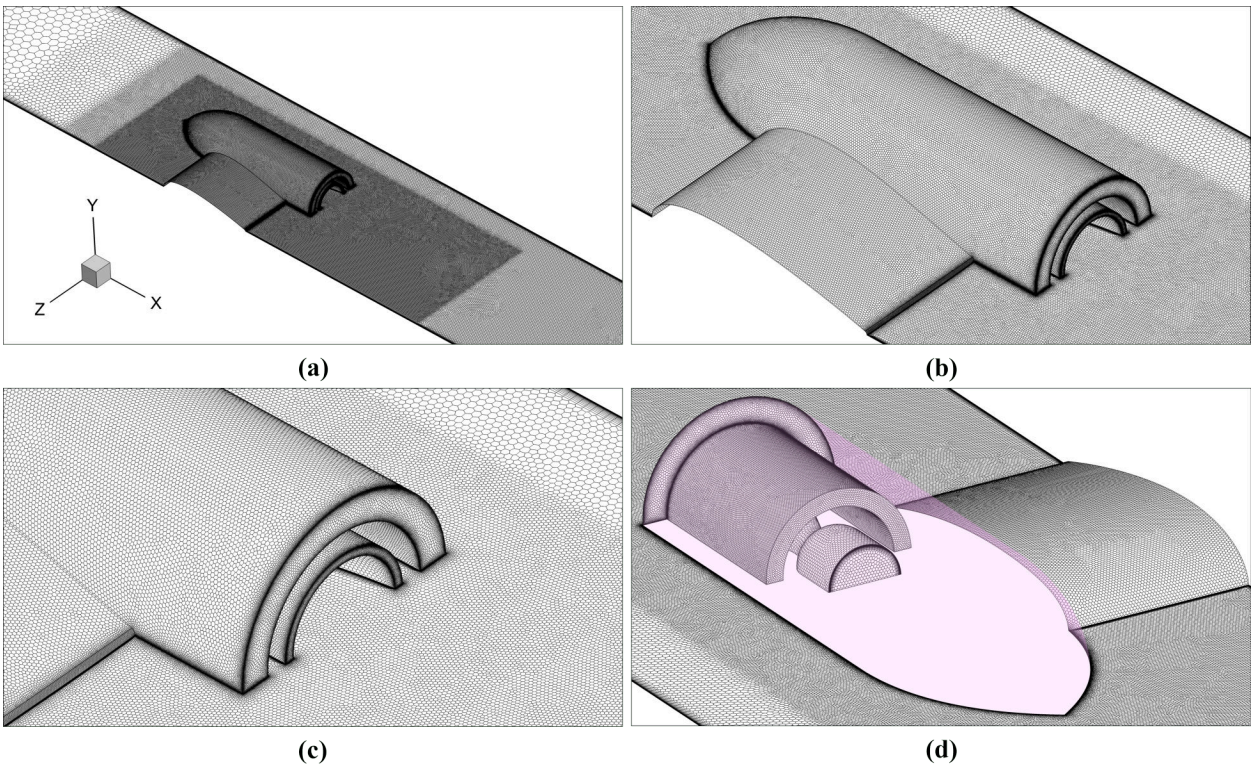

Fig. 5 Surface mesh on: (a) model and symmetry plane, (b) nacelle and pylon, (c) close-up view on base region, (d) close-up view on cavity and nozzle

accounts for both the forces exerted on the body as well as the standard gross thrust (Eq. (7)). As shown in Table 1, the GCI corresponding to the medium mesh for the standard velocity coefficient is 0.42%, while the GCI for the GPF is 0.68%. The apparent order p, is close to the formal order of the employed discretization scheme (2^{nd}), which can be taken as a good indication of the grids being in the asymptotic range [42]. The computational cost of the finest grid is increased by a factor of 5 compared to the medium grid, which would translate into an increase by an order of magnitude in the total wall-time for all computations. Consequently, based on the results of the grid convergence analysis as well as on the computational cost, grids of approximately 13.7 million cells were used.

Computations used an implicit, density-based and compressible Reynolds-averaged Navier-Stokes solver [43], coupled with the $k-\omega$ SST turbulence model [44], which has been found to perform reasonably well for over-expanded nozzle flow cases [45] as well as for powered-on, after-body flows with separation [46]. Roe's approximate Riemann solver was used for the calculation of the convective fluxes [47]. Due to the polyhedral topology of the grid, a Green-Gauss cell-based method was employed to calculate the flow-field gradients, to avoid the increased computational cost of a node-based approach. A second-order accurate upwind scheme was used for discretization of the flow primitive variables as well as for turbulent kinetic energy k and specific dissipation rate ω. Variable gas properties were employed using an 8^{th} order piecewise polynomial for the calculation of specific heat capacity as a function of static temperature [48]. Thermal conductivity κ was computed according to kinetic theory [43], while the dynamic viscosity was calculated based on Sutherland's law [49].

IV. Results and discussion

A. Installed design space

In order to shape the design space of the experimental campaign, it is necessary to establish the function(s) describing the correlation between the key variables that drive wind tunnel operation and those that are of aerodynamic interest. Rigorous use of computational fluid dynamics allows to extract this correlation well in advance of any experimental

Table 1 Calculation of discretization error

	ϕ = standard velocity coefficient $C_{V,s}$ (monotonic convergence)	ϕ = gross propulsive force over GPF_{fine}(monotonic convergence)
N1, N2, N3	44M, 13.7M, 3M	44M, 13.7M, 3M
r_{21}	1.476	1.476
r_{32}	1.647	1.647
ϕ_1	0.9501	1.0000
ϕ_2	0.9469	0.9928
ϕ_3	0.9377	0.9681
p	1.79	2.11
ϕ_{ext}^{21}	0.9533	1.006
e_a^{21}	0.34%	0.72%
e_{ext}^{21}	0.33%	0.54%
GCI_{fine}^{21}	0.42%	0.68%

testing, and serves to highlight potential favorable regions or practical limitations. In the context of this work, it is critical to translate the operational parameter of TPR, into the aerodynamic parameter of interest, which is the approach Mach number M_a, for each setting of the exhaust (i.e., each NPR). Prior knowledge of this correlation is nearly impossible, owing to the strong influence of the blockage ratio and nozzle settings. Figure 6 shows the variation of the approach Mach number M_a, measured at the tunnel inlet, as a function of the design variables, namely TPR and NPR. Data from an experimental activity in the TSWT, operating nearly empty ($BR \sim 0.3\%$) are superimposed on the graph of Fig. 6, along with the curve corresponding to fully isentropic flow. A very good correlation between the experimental data and the isentropic law can be seen, indicating that under very low BRs, the losses within the tunnel are negligible. However, the numerical results from the tunnel-installed model, show that under the high blockage ratio of approximately 16.5%, the approach flow conditions ($M_a = f(TPR, NPR)$) deviate significantly from the low BR case, highlighting the influence of blockage effects. As shown in Fig. 6, for TPR above values of approximately 1.52, the flow within the wind tunnel is choked owing to the high BR, and M_a gets invariant to further increase of TPR or NPR. The maximum approach Mach number that can be achieved within the examined design space is approximately

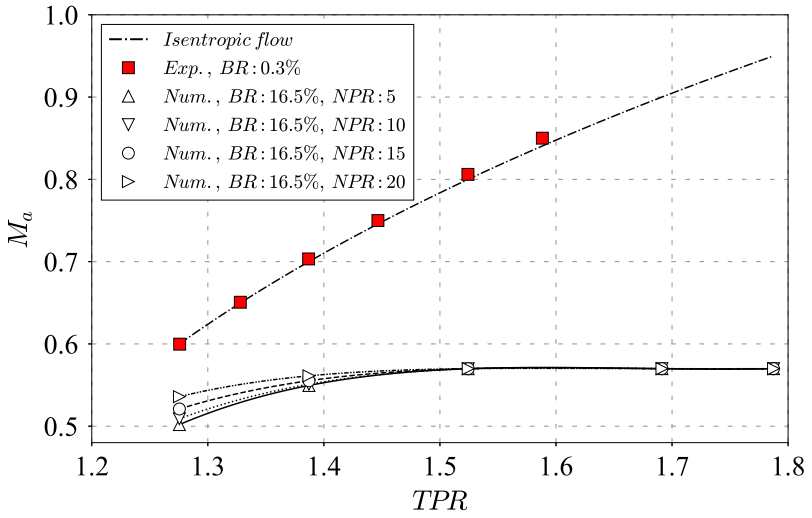

Fig. 6 Variation of approach Mach number M_a within the examined design space

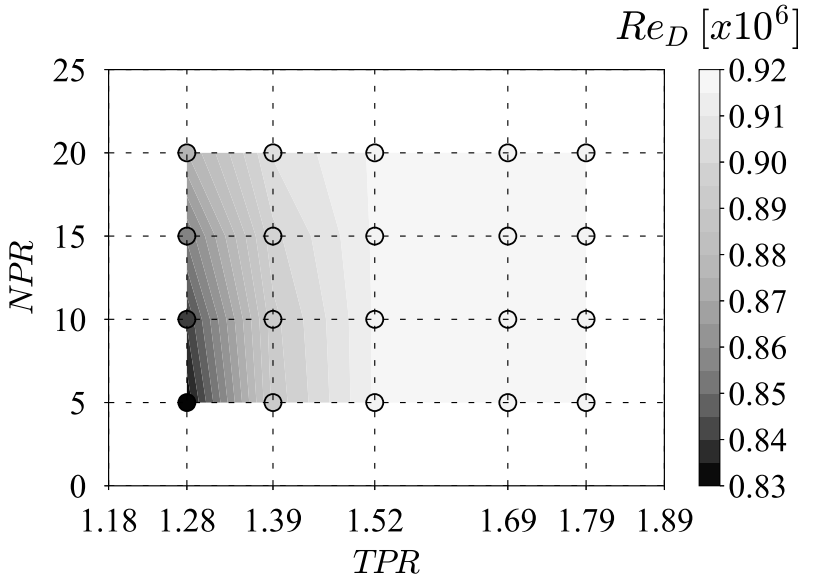

Fig. 7 Variation of Re_D in the examined design space; Re_L lies within the range of $2.59 \cdot 10^6 < Re_L < 2.86 \cdot 10^6$

M_a=0.57. At pre-choking conditions, the jet flow of the propulsive nozzle has a clear effect on the approach Mach number, which increases with increasing NPR for fixed $TPRs$. This is owing to the relatively high total pressure flow which is being injected in the wind tunnel. This effect is more intense at low $TPRs$ and gradually diminishes as the flow approaches the choking point.

Figure 7, depicts the variation of the Reynolds number at the tunnel inlet based on the model's diameter D, as a function of NPR and TPR. The exact conditions of the cases examined are indicated with circles of varying color according to the corresponding value of Re_D. The effect of choking is clearly visible after TPR values of approximately 1.52, fixing the maximum achievable Reynolds number to values of $Re_D = 0.92 \cdot 10^6$ or accordingly $Re_L = 2.86 \cdot 10^6$ based on the maximum length of the model. Additionally, at pre-choking conditions, the behavior of Reynolds number is dominated by TPR settings rather than NPR, which has a minor effect. At post-choking conditions, NPR has no effect on the approaching flow Reynolds number. Both Figs. 6 and 7 demonstrate the limitations in terms of maximum M_a and Re_D within the examined range of TPR. Additionally, the region where the experimental measurements are expected to be reasonably valid with respect to equivalent free-stream conditions in terms of flow similarity are shaped, namely in the range of $1.28 < TPR < 1.52$.

This analysis demonstrates that for reasonably high BRs, it is practically unfeasible to produce free-flight-equivalent conditions of transonic (and even high subsonic) flow in a closed wind tunnel. In fact, based on one-dimensional isentropic flow assumption, achieving transonic approach Mach numbers of M_a=0.9 and 0.95, would require the blockage ratio to be drastically reduced to values of BR=0.88% and 0.21%, respectively [31]. Realizing that these values of BR are very impractical, it is essential to assess the extend of global and local flow similarity with respect to unbounded flow under relatively high BRs which are often encountered, especially in academic facilities. It is stressed that local flow similarity is somewhat irrelevant when overall aerodynamic performance is of interest, but is critical in the context of base flows. In what follows, both global and local flow characteristics are discussed.

B. Global flow characteristics

Figure 8 illustrates the flow Mach number distribution in the tunnel, at the upper and lower limit conditions of the design variables, NPR and TPR (i.e., $NPRs$ of 5 and 20, and $TPRs$ of 1.28 and 1.79, respectively). Observing Figs. 8a and 8b, the effect of NPR on the base flow for fixed TPR=1.28 can be seen. A higher flow expansion is visible at the model's shoulder and base, as a result of increased NPR, indicating a higher approach Mach number, in line with the results shown in Fig. 6 at pre-choking conditions. The choked flow conditions as a result of increased TPR are also shown in Figs. 8c and 8d. In both cases, a clear flow expansion to supersonic speeds is visible at the vicinity of the base of the model, which coalesces into a compression shock further downstream. In the case of NPR=20 (Fig. 8d), the

expansion is intensified, resulting in a stronger compression shock, which reflects on the top tunnel wall and generates a severe, shock-induced flow separation. The flow conditions under chocked tunnel operation, are strongly affected by the surrounding tunnel walls and pylon, and clearly do not represent free-stream transonic conditions, even though at the vicinity of the base, the flow can get locally transonic. This further supports the argument that there is a region of the examined design space at post-choking tunnel operation, where experimental data could be meaningful for validation of numerical results, but could not correlate to actual unbounded flow conditions. This highlights the limitations that are posed upon the initially designed analysis based on free-stream numerical simulations, due to practical reasons such as model fabrication and instrumentation as well as wind tunnel integration effects. Additionally, in Fig. 8 asymmetrical flow in the xz plane is visible for all cases, and manifested specifically in the flow exiting the propulsive nozzle through a jet vectoring effect. This is substantially intensified at post-choking flow conditions (Figs. 8c and 8d). This tilting phenomenon of the jet was consistent in all examined cases and further analysis on its behavior and origins is performed and discussed in the following section.

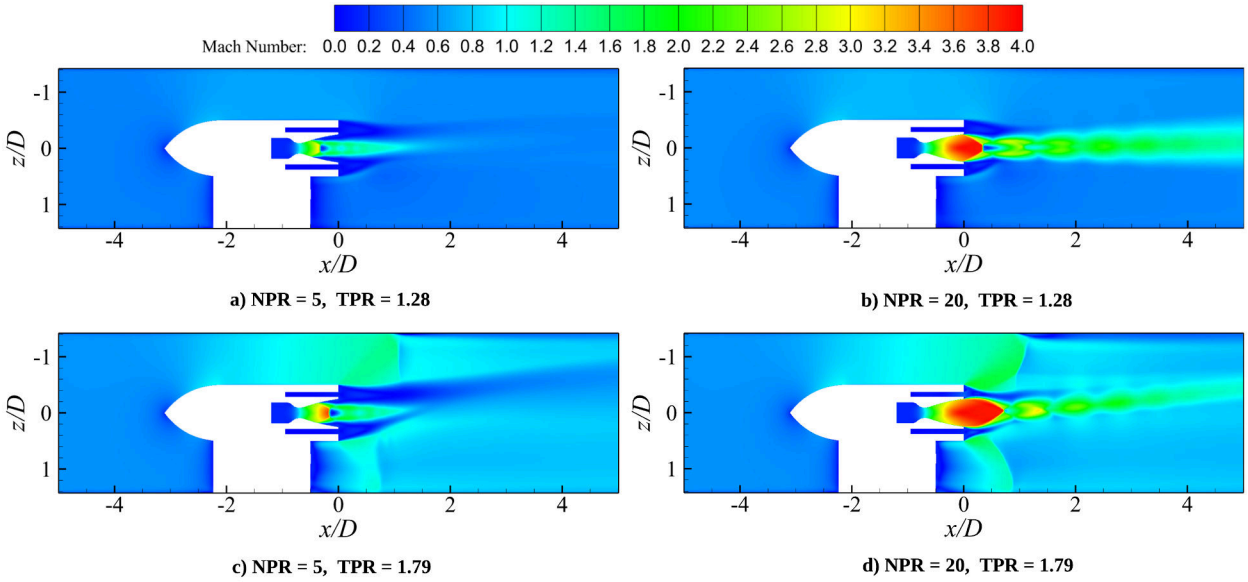

Fig. 8 Distribution of Mach number as a function of NPR and TPR

1. Jet vectoring effect

In order to evaluate the behavior of the jet vectoring effect within the investigated design space, a well-defined and systematic metric is required. This is facilitated through the definition of the jet angle a_j, as shown in Fig. 9. The slope of the axial streamline (annotated with white color in Fig. 9) varies spatially and is highly dependent on the corresponding flow conditions. To overcome this ambiguity and establish consistency between the different cases, the jet angle is defined as the angle between the axial line, and a line passing through the center point of the nozzle's exit plane and a point located 15 diameters D downstream of the base (i.e., points P_1 and P_2 respectively in Fig. 9). In this sense, only the radial location z/D of point P_2 can vary, thus providing a quantification of the axial streamline deflection with respect to the axis. With these provisions, the jet angles are extracted and compared for each case within the examined design space.

Figure 10 illustrates the variation of the jet angle a_j as a function of TPR and NPR. The conditions corresponding to choked tunnel operation are also annotated. A systematic trend can be observed, of decreasing jet angle with increasing $NPRs$ for all investigated $TPRs$. This is owing to the higher flow expansion that is achieved which allows the jet flow to be less sensitive to pressure distribution asymmetries in the xz plane. This trend is not particularly true for the TPR_{max}=1.79 case, where the jet angle is approximately the same for $NPRs$ of 5 and 10. Given the highly unsteady nature of these cases, this is attributed to the inability of a RANS-based approach to accurately quantify these effects, and does not invalidate the overall observed trend of reducing jet angle with increasing NPR. The effect of TPR on the jet angle for fixed $NPRs$ is also shown in Fig. 10. At pre-choking conditions (i.e., TPR<1.52) the trend is systematic for

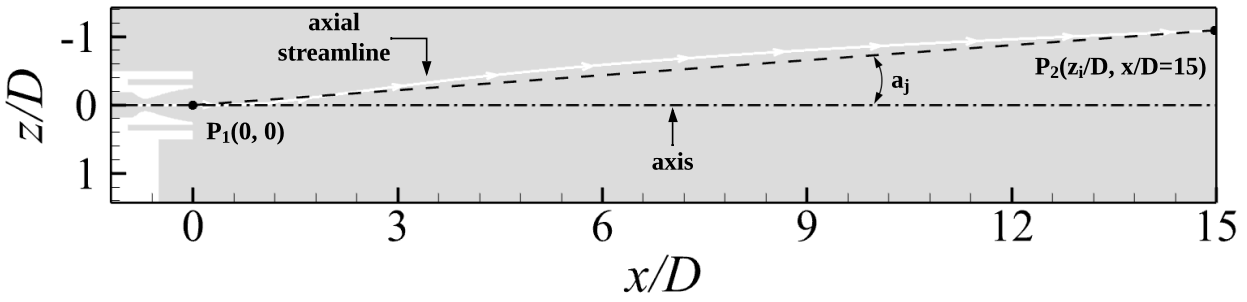

Fig. 9 Definition of jet angle a_j; The axial streamline shown corresponds to NPR=15 and TPR=1.69

the cases of NPR=10, 15 and 20, where the minimum angle is achieved at TPR=1.39, while higher or lower values of TPR would increase the jet angle. Especially in the case of NPR=20 and TPR=1.39, the jet angle is approximately zero. However, this should not be interpreted as the flow being symmetric. On the contrary, these trends demonstrate that the jet vectoring effect is dynamically affected by both wind tunnel settings and nozzle pressure ratios. For the NPR=5 case, an almost-linear correlation of decreasing jet angle with increasing TPR can be seen at pre-choking conditions. This could be associated with the jet flow being highly over-expanded at this NPR (Fig. 8a), and suggests that the flow asymmetry in the pylon-parallel plane is affected by a combination between the degree of expansion that is achieved in the nozzle, and the surrounding wind tunnel flow. Additionally, a clear, discontinuous jump in the jet angles for values of $TPRs$ above 1.52 is visible in Fig. 10 for all $NPRs$, suggesting that choking has an impact on the jet vectoring effect. This analysis further implies that the conditions corresponding to choked tunnel operation cannot be relied upon for reasonable experimental data, owing to the intensified jet angles, which will substantially modify the aerodynamic behavior of the system and will probably not be present in a free-stream flow simulation. Furthermore, it demonstrates the importance of a rigorous numerical analysis to support the design of experiments procedure, before proceeding with the experimental activities.

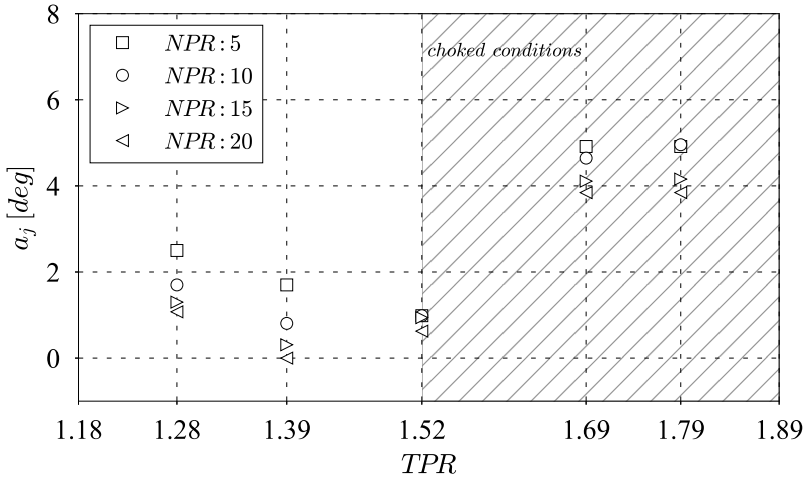

Fig. 10 Variation of jet angle a_j with TPR and NPR

2. Impact of pylon on the jet

The previously discussed jet vectoring effect, must be further analysed in order to identify its underlying mechanism. This is facilitated through the numerical simulation of an identical propulsive configuration, where the effect of the tunnel walls is eliminated. In specific, a modified computational domain is constructed (not shown here for brevity), where the surfaces originally corresponding to the top and side tunnel walls (Fig. 1), are extended at a distance equal to 10 times the length of the model L. A pressure far-field BC is applied on these surfaces to model the free stream

conditions with the ambient static pressure and temperature, as well as the free stream Mach number as the prescribed values. Similarly, on the surfaces originally corresponding to the tunnel inlet and outlet, the same pressure far-field BC is applied. On the surface that corresponds to the bottom tunnel wall (Fig. 1), a symmetry BC is applied, assuming that the effect of a symmetric jet flow will be negligible, which is expected to be valid especially at low $NPRs$. This approach allows for the identification of the impact of the pylon on the base flow, and eliminates any potential effect of the tunnel walls. It should be noted, that for post-choking tunnel conditions, the global flow similarity with respect to free-stream flow is practically non-existent, and matching the two approaches to establish consistency in the comparison is far from trivial. For that reason, the comparison is performed for a well-behaved case, corresponding to pre-choking tunnel conditions and medium NPR, namely TPR=1.28 and NPR=10. For that case, the free stream Mach number for the modified domain is matched to the approach Mach number for the tunnel-installed case. The numerical approach is identical to the one described previously for the wind tunnel flow simulations. The computational mesh employs the same number of prism layers on the wall surfaces of the model (35), as well as identical spatial discretization and grid refinement regions. The remainder of the modified domain is populated with polyhedral elements of size equal to the maximum element size in the original domain.

Figure 11 depicts the Mach number distribution for the modified, free-stream flow case (top) and the tunnel-installed case (bottom). It is clearly obvious, that the jet vectoring effect still manifests in the absence of the walls of the wind tunnel, ensuring that the origin of this phenomenon is the asymmetry caused by the existence of the pylon. The jet angle a_j, is also annotated in the figure for both cases. Even though the jet vectoring effect is still present in the free-stream case, the jet angle in the tunnel-installed flow is 30% higher. It should be stressed, that RANS computations are not reliable in accurately quantifying such variations and should be treated with caution. However, additional differences can be observed between the two cases. In specific, the achieved flow expansion on the shoulder of the nacelle is higher in the tunnel-installed case as a result of the effect of the tunnel walls [34], leading to a lower pressure distribution at the vicinity of base and near-wake region, in the upper part of the domain (i.e., z/D<0). This could explain the higher jet angle of the tunnel-installed case, and is in line with the discontinuous increase in the jet angle values for choked tunnel operation (Fig. 10). However, to reach this conclusion, further analysis is required, involving comparative assessment of additional test cases between the two conditions.

Observing the employed computational mesh in Fig. 5, it could be argued that the asymmetry in the discretization might have an effect on the jet vectoring phenomenon. In specific, the computational grid features increased spatial resolution downstream of the pylon compared to the region between the base and top tunnel wall (z/D<0). This is related to the increased discretization requirements due to the flow separation that occurs upstream of the pylon trailing edge and corresponding wake, which could impact the base flow. To address this argument, the pylon was removed from the computational domain, making the configuration axially symmetric, while maintaining identical, non-symmetric meshing approach as the one for the installed model. The computational mesh for this case was slightly smaller as a result of the absence of the pylon. Figure 12 shows the Mach number distribution at conditions of TPR_{max}=1.79 and NPR_{max}=20 for the installed case (top) and the case corresponding to axially symmetric configuration (bottom). It is

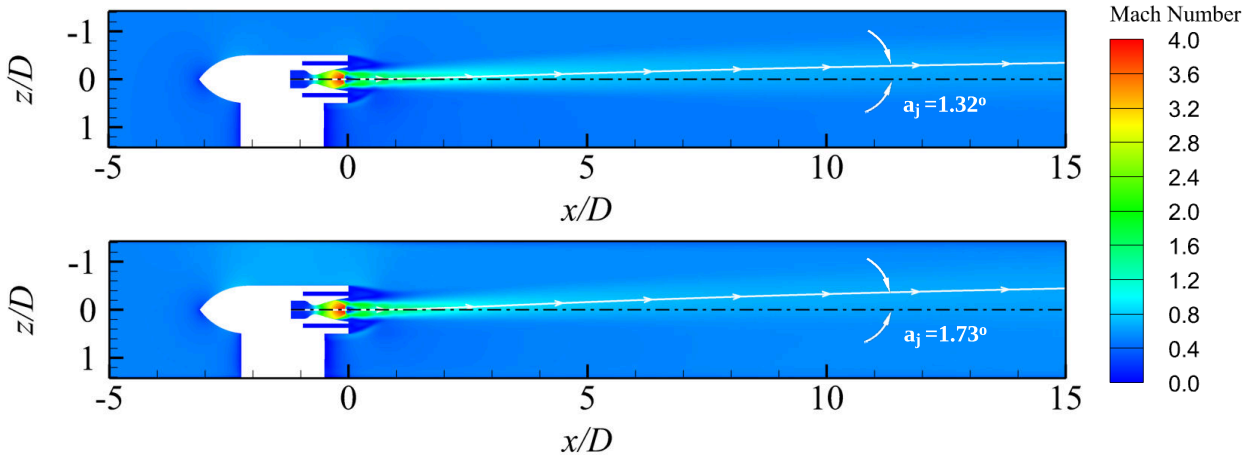

Fig. 11 Mach number distribution for free-steam (top) and tunnel-installed (bottom) cases (NPR=10, TPR=1.28)

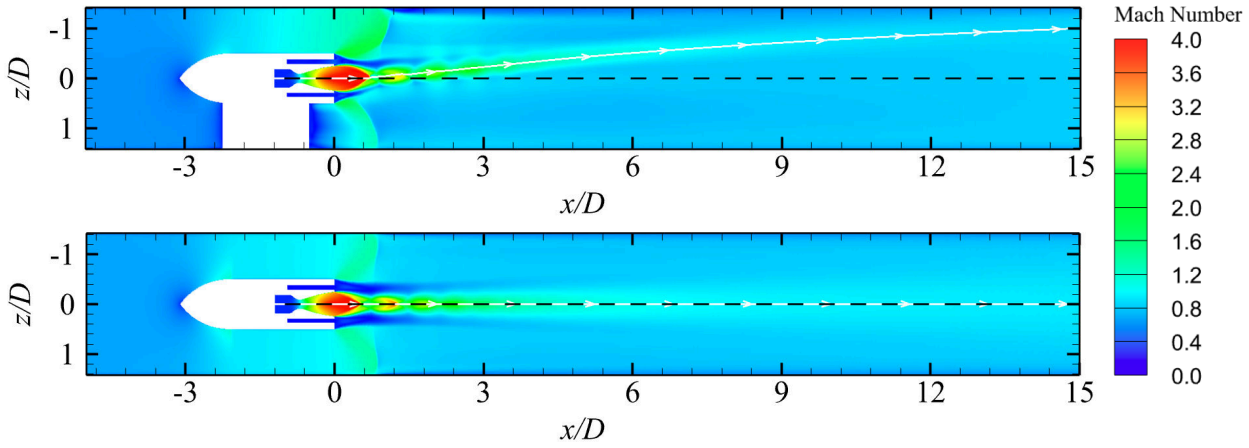

Fig. 12 Mach number distribution at TPR=1.79 and NPR=20 for the installed (top) and no-pylon (bottom) cases

shown that the no-pylon case features a fully-symmetric flow topology even at post-choking tunnel conditions, and the propulsive jet is not vectored, regardless of the asymmetry in the computational grid. Furthermore, it is demonstrated that tunnel choking has no effect on the symmetry of the surrounding flow at the absence of the pylon. However, once flow asymmetry is established through the pylon, tunnel choking seems to intensify its impact on base flow (Fig. 10).

The analysis presented in this section clearly shows that the jet vectoring effect is the result of the asymmetry in pressure distribution caused by the pylon, while there are indications that post-choking tunnel operation could potentially intensify this effect. Additionally, the asymmetry that is caused by the pylon, is linked with the associated flow separation, and therefore, further studies on the impact of the pylon characteristics on the jet angle should be carried out (e.g., pylon thickness, swept-wing configuration, etc.). Regardless, these results suggest that this effect could potentially manifest to some extend, in any severely separated base flow of wing-tip mounted nacelle configurations, which are often employed in several, high-speed propulsion concepts [1, 7].

C. Local flow characteristics

The preceding analysis focused on the effects of wind tunnel installation on the global flow characteristics of the investigated apparatus. Even though there is indeed a region of the design space corresponding to pre-choking operation where experimental measurements could potentially be corrected to represent unbounded-equivalent flow conditions, the application of such corrections for a complex configuration, which is strongly influenced by blockage effects, as well as nozzle and tunnel settings, is far from trivial and could be quite intricate. Additionally, as discussed previously, such installation effects due to high blockage can be quite common in academic facilities, owing to the combination of small wind tunnels [29] and the requirement for a relatively large model. However, in the context of base flows, it is usually the local flow characteristics at the surface of the base that are of critical importance [14, 23, 27]. Consequently, it is vital and of high practical value, to investigate whether a tunnel-constrained flow could feature local flow similarity at the base with respect to equivalent, unbounded flow conditions, even if the global flow topology differs notably. In this study, a systematic approach to address this question is employed and presented in this section.

1. Rationale

Herein, base flow similarity is examined between the model installed in the TSWT and an identical, axially symmetric geometry corresponding to unconstrained flow conditions. Installation effects caused by the pylon, tunnel walls and blockage are totally removed from the free-stream case. Therefore, a two-dimensional, axisymmetric computational approach is employed for the free-stream case, using an implicit, density-based and compressible, RANS solver [43]. The numerical approach adopted for this analysis is identical to the one described previously for the three-dimensional, tunnel-installed model. The domain is discretized using a multi-block, fully structured grid approach [50]. The computational domain, boundary conditions as well as meshing approach, are adopted from previous work [27], involving an identical configuration under free-stream conditions, featuring a slightly modified cavity shape. Figure 13 shows the computational mesh employed for this study (left) along with a close-up view on the cavity and nozzle regions

(right). The GCIs [42] corresponding to the medium mesh for the drag and nozzle standard velocity coefficients (C_d and $C_{V,s}$), are 0.26% and 0.75%, respectively. Consequently, the medium grid of approximately 1.2 million cells is employed [27].

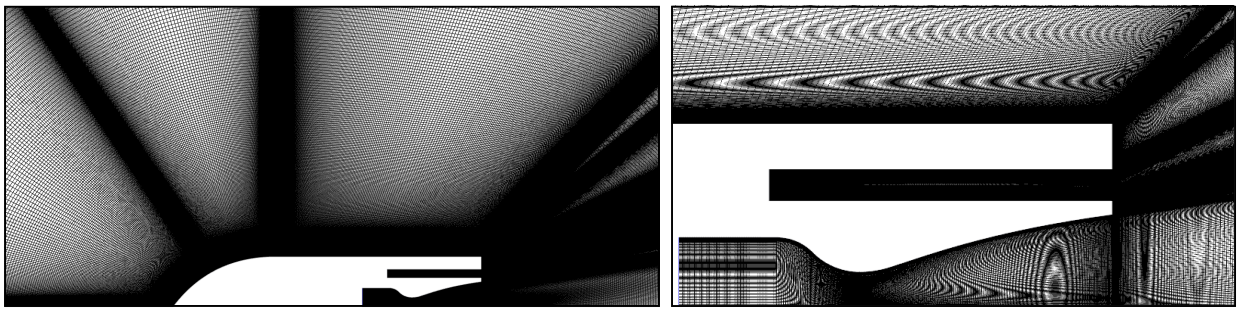

Fig. 13 Mesh employed for unconstrained flow conditions (left) and colse-up view on base region (right)

Wind tunnel installation effects and high blockage in specific, notably affect the flow surrounding the model in the tunnel, even at pre-choking conditions [31] as shown previously (Fig. 6). This makes the comparison between the two cases in terms of flow conditions, anything but straightforward. In other words, there is no way to know a priori what are the conditions that need to be prescribed in the unbounded, free-stream case (i.e., M_∞), to match the conditions in the vicinity of the base of the model in the tunnel. In this study, we propose a methodology to allow for proper comparison of the base flows between the tunnel-constrained and equivalent unbounded flow cases. The approach is based on systematic comparison of the static pressure distribution at the surface of the base, which is critical in experimental base flows and base drag analysis in specific [23, 26]. The employed metric of interest, on the basis of which the analysis is established, is the effective Mach number immediately upstream of the base, denoted as M^b_{eff} and defined in Eq. (8):

$$M^b_{eff} = \left[\frac{2}{(\gamma - 1)} \left(\left(\frac{P_0}{p^b_\phi} \right)^{\frac{\gamma-1}{\gamma}} - 1 \right) \right]^{\frac{1}{2}} \tag{8}$$

This is the Mach number that would be achieved theoretically, under isentropic flow assumption, depending on the pressure ratio between the total pressure P_0 and the local static pressure p^b_ϕ on the nacelle shoulder, immediately upstream of the base surface. The subscript ϕ indicates the corresponding azimuthal angle in the yz plane (Fig. 1), where the pressure value is extracted ($0<\phi<180$) for the tunnel-installed model. The total pressure P_0 in Eq. (8) is atmospheric for both free-stream and tunnel-constrained cases. Consequently, M^b_{eff} represents directly the local static pressure at the end of the afterbody flow expansion, and allows to map the design space variables for each case at a given NPR, through the functions $M^b_{eff}=f(TPR)$ and $M^b_{eff}=f(M_\infty)$, respectively. Therefore, this approach allows for a comparison to be made on the basis of a local flow similarity parameter, namely M^b_{eff}, and hence, to quantify to what extend the base pressure distribution is similar. This methodology could be applied to any base flow analysis, for both power-off and power-on configurations.

2. Base flow mapping

The analysis initially requires knowledge of the achieved flow expansion at the model shoulder in the free-stream case, that is, construction of the mapping function $M^b_{eff}=f(M_\infty)$ for a given NPR. For this analysis, a medium NPR of 10 is selected for both tunnel-constrained and free-stream cases, as it includes both high and low degrees of over-expansion within the range of $1.28<TPR<1.79$. A sweep of M_∞ values is performed for the unbounded flow, in the range of $0.5<M_\infty<1.5$ with a step of 0.05, producing a total number of 21 cases. The effective Mach number is extracted for each M_∞ case as the average value across a length corresponding to approximately three computational cells upstream of the base. This is done to avoid numerical instability and discontinuity at the singularity formed between the shoulder and base surfaces (Fig. 1). The same procedure is applied for the tunnel-installed cases corresponding to a sweep of $TPRs$ in the range $1.28<TPR<1.79$ and $NPR=10$ as shown in the design space definition in Fig. 2, to retrieve the mapping function $M^b_{eff}=f(TPR)$. In this case, M^b_{eff} is an average of the effective Mach numbers, extracted at six different

azimuthal locations as shown in Fig. 14 (ϕ=0°, 45°, 90°, 135°and 180°) to take into account three-dimensionality effects caused by the blockage, tunnel walls and pylon.

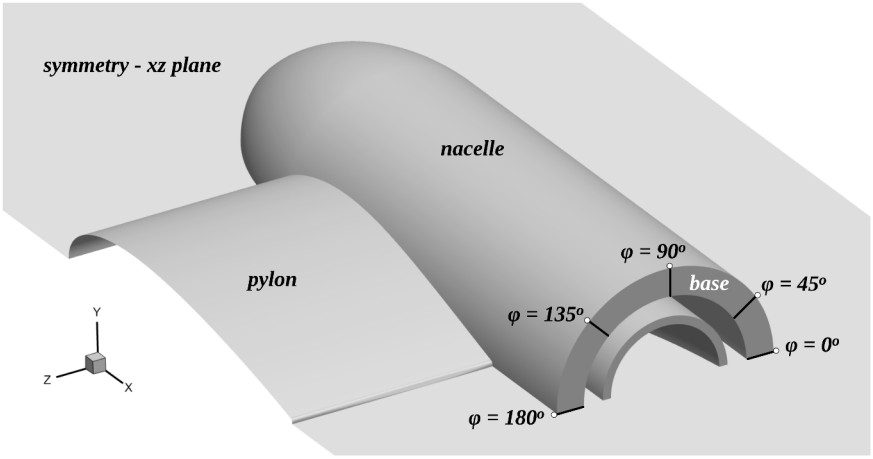

Fig. 14 Azimuthal angles ϕ along the base surface

Figure 15 depicts the mapping of free-stream Mach numbers M_∞, to tunnel pressure ratio settings TPR, for NPR=10, on the basis of the effective Mach number at the base. For the free-stream case, the trend of the flow expansion at the nacelle and afterbody, described through the correlation of $M^b_{eff}=f(M_\infty)$, is modified above supersonic M_∞ values. Therefore, it is split between the regions corresponding to subsonic and supersonic free-stream flow conditions (i.e., $0.5\leq M_\infty<1$ and $1\leq M_\infty\leq 1.5$). Through the mapping shown in Fig. 15, it is now possible to retrieve the free-stream conditions that would produce the same M^b_{eff} at any given setting of TPR. This method is essential in order to establish proper base flow similarity comparison between tunnel-constrained and unbounded flow cases, since there is no straightforward approach that allows a priori matching of the conditions at the vicinity of the base.

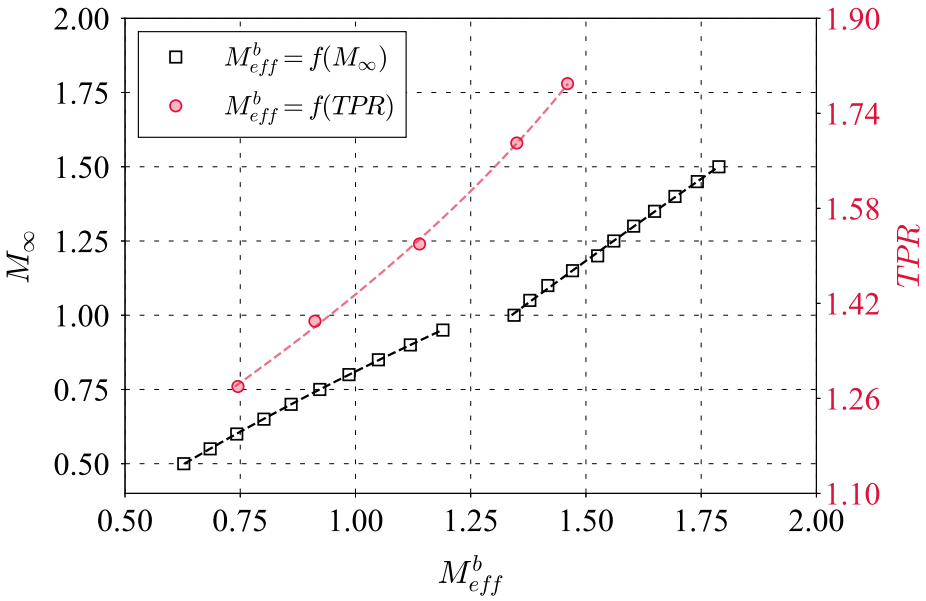

Fig. 15 M_∞-TPR mapping on the basis of M^b_{eff} for unbounded and tunnel-constrained flows at NPR=10

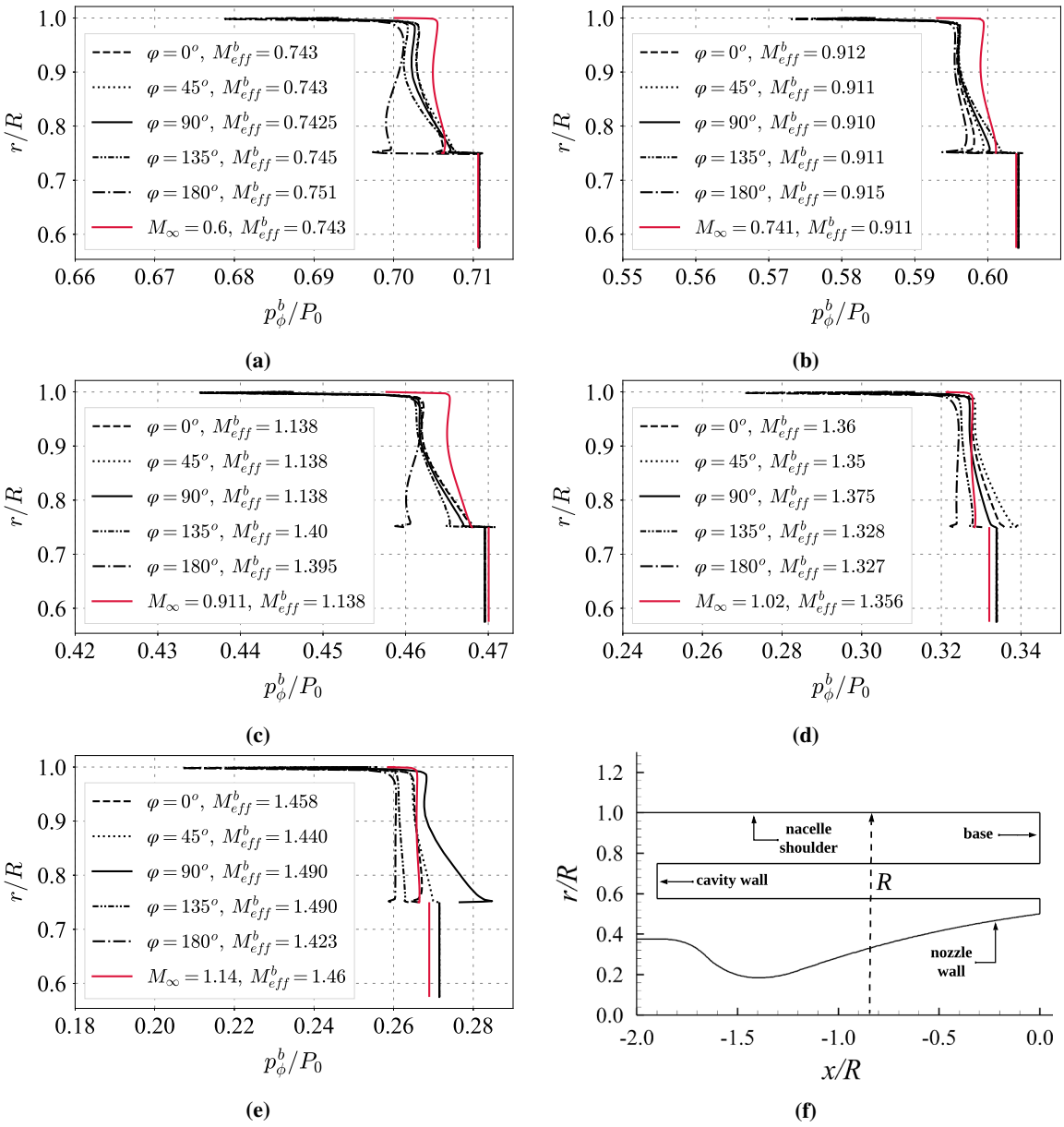

Fig. 16 Base pressure distribution for tunnel-installed and free-stream cases at NPR=10: (a) TPR=1.28, (b) TPR=1.39, (c) TPR=1.52, (d) TPR=1.69, (e) TPR=1.79 and (f) base geometry schematic

3. Base flow similarity comparison

Based on the mapping methodology described above and illustrated in Fig. 15, the free-stream Mach number of the unbounded flow, is adjusted to match the azimuthal average M^b_{eff} (within ≤0.6%) for each examined TPR (i.e., TPR=1.28, 1.39, 1.52, 1.69 and 1.79 for NPR=10 in Fig. 2). The pressure distribution at the base is then compared between the free-stream and tunnel-constrained flows to assess the local flow similarity characteristics. Figures 16a through 16e show the variation of p^b_ϕ/P_0 along the surfaces of the cavity side wall and base for each corresponding TPR value. The radial location r where the surface pressure data is taken and compared, non-dimensionalized over the model's radius R, is shown in Fig. 16f ($0.575<r/R<0.75$ for the cavity wall and $0.75<r/R<1$ for the base). For the wind tunnel case, base pressure distribution at all six azimuthal angles is included (ϕ=0°, 45°, 90°, 135°and 180°), to assess three-dimensionality effects as a result of the high blockage ratio, as well as tunnel walls and pylon interference.

Observing Fig. 16, it can be seen that local flow expansion characteristics at the edge formed between the nacelle

shoulder and the base surface exhibit some differences in the case of the tunnel compared to unbounded flow conditions. In specific, for all $TPRs$ examined, the flow in the wind tunnel expands further to lower pressures just downstream of the nacelle shoulder (i.e., $0.995<r/R<1$) before pressure recovery initiates, owing to the high blockage effect. On the contrary, in the free-stream case, and conditions corresponding to subsonic flow (Figs 16a, 16b and 16c), pressure recovery initiates immediately at the base. The pressure distribution of the wind tunnel case deviates and recovers to reduced levels with respect to the free-stream case. This deviation is increased at higher radial locations (i.e., close to the edge of the nacelle shoulder) and gradually diminishes as the radial location decreases. In fact, the base pressure distribution along the cavity wall ($0.575<r/R<0.75$) for $TPRs$ corresponding to pre-choking tunnel conditions (Figs 16a, 16b and 16c), agrees within less than 0.1% with respect to the equivalent unbounded flow. Additionally, the trend of pressure recovery distribution at the base between the two conditions is similar (except for ϕ=180^o which is directly downstream of the pylon). The initial expansion region in the wind tunnel ($0.995<r/R<1$) corresponds to less than 1.5% of the total examined base surface area (including the cavity wall) and its actual length is smaller than the size of most miniaturized dynamic pressure transducers by a factor of 5, which makes it irrelevant in the context of experimental measurements. Neglecting this region, the maximum deviation at pre-choking conditions in the range of $0.575<r/R<0.995$ (i.e., above 98.5% of the base surface area) and $0^o<\phi<135^o$, is less than 0.7%. This deviation can increase by a factor of 2 to values of approximately 1.5% at the base region directly downstream of the pylon, as indicated in Figs. 16a and 16c with the lines corresponding to azimuthal angle ϕ=180^o. In all examined TPR cases, the base pressure in the region downstream of the pylon (ϕ=180^o) recovers to reduced levels compared to the rest azimuthal locations. This demonstrates the strong interference effects caused by the presence of the pylon, especially at pre-choking conditions (Figs 16a, 16b and 16c).

For the cases corresponding to post-choking tunnel operation, namely TPR=1.69 (Fig. 16d) and 1.79 (Fig. 16e), a notable deviation in the azimuthal pressure distribution can be seen along the base surface ($0.75<r/R<1$) of the tunnel-installed model, which becomes more intense closer to the cavity. The maximum deviation of approximately 7.5% in the base pressure distribution of the tunnel-installed model, is found at TPR_{max}=1.79 between angles of ϕ=90^o and 180^o. These are the azimuthal locations where the side tunnel walls are closer to the model (ϕ=90^o) and directly downstream of the pylon (ϕ=180^o) respectively. However, the pressure at the cavity wall recovers to the same values regardless of the azimuthal angle ϕ, for both post-choking TPR values of 1.69 and 1.79 (Figs 16d and 16e). The base pressure distribution of the equivalent, unbounded flow corresponding to the post-choking tunnel cases, falls within the azimuthal pressure range of the tunnel-constrained flow as shown in Figs. 16d and 16e. The maximum deviation in base pressure between the unbounded and tunnel-installed flow conditions for the $TPRs$=1.69 and 1.79 cases, is approximately 3.25% and 6.5%, respectively, identified closer to the cavity ($\sim r/R$=0.75). However, the pressure distribution along the cavity wall for the unbounded flow agrees within less than 0.57% and 1% with respect to the tunnel-constrained flow, for the $TPRs$=1.69 and 1.79 cases, respectively.

This analysis shows that the base pressure distribution of the free-stream flow compares reasonably well with respect to tunnel-constrained flow conditions, where the effective Mach numbers at the base have been matched through the methodology presented above. In specific, for pre-choking tunnel conditions, pressure distribution similarity of less than 1.5% can be achieved in the base surface ($0.75<r/R<0.995$), while in the cavity wall ($0.575<r/R<0.75$), this improves by an order of magnitude ($< 0.1\%$). At post-choking conditions, the pressure distribution corresponding to unbounded flow, is still within the azimuthal range of the tunnel-installed case, but deviations can reach values up to 6.5%. This is not unexpected, since the deviations in azimuthal base pressure distribution corresponding to such tunnel flow conditions can be as high as 7.5%, indicating the strong tunnel-installation effects. Even at such conditions, the pressure distribution on the cavity wall, agrees with the equivalent free-stream flow within less than 1%. This means that local base flow similarity can be established between tunnel-installed and free-stream flow conditions, on the basis of the effective Mach number at the base, M^b_{eff}, even if the global flow characteristics are notably different in the two flows.

V. Conclusions

A numerical investigation of wind tunnel installation effects on the overall base flow characteristics for a generic, high-speed exhaust system, featuring a cold flow, TIC nozzle along with an axisymmetric cavity region at the base, is presented in this study. The examined configuration is considered representative of future, high-speed propulsion concepts, usually employing base-embedded nozzles and cavities. Three-dimensional Reynolds-averaged Navier-Stokes computations are employed to perform an aerodynamic analysis on the global and local flow characteristics of the tunnel-installed model. This facilitates an ongoing design of experiments activity and serves to identify any potential limitations in advance.

Results show that the high blockage ratio of 16.5% limits the viable design space of the installed model to approach Mach numbers of approximately 0.57 before the flow is choked in the tunnel. The increase of NPR for pre-choking conditions leads to higher approach Mach numbers for the same TPR, owing to the increased total pressure of the added jet flow. A systematic jet vectoring effect is identified for all cases examined as a result of the pressure distribution asymmetry in the afterbody and near-wake flow. This is increased at low NPRs. The origin of this effect is investigated and found to be caused solely by the existence of the pylon. However, the jet angle increases discontinuously after choking conditions, thus suggesting that choking might further intensify the jet vectoring effect. This result suggests that the tilting phenomenon of the jet could manifest to some extent, in any separated base flow of wingtip mounted nacelle configurations, which are often employed for future, high-speed propulsion systems, and thus, further studies should be conducted on this effect.

Additionally, local base flow similarity is examined between the tunnel-installed model and unconstrained, free-stream flow conditions for an identical, axisymmetric geometry. Proper comparison between the two cases is far from trivial due to three-dimensionality effects in the wind-tunnel, especially for post-choking conditions. Therefore, a methodology is presented to establish comparability between the two cases, based on the effective Mach number at the base. This method can be applied to any base flow analysis, for both power-on and power-off configurations. It is shown that for pre-choking conditions, the pressure distribution on the base agrees within less than 0.7%. This can increase up to 1.5% for the location downstream of the pylon (ϕ=180^o). The similarity in pressure distribution improves by an order of magnitude to values of 0.1% on the cavity wall. At post-choking conditions, the distribution of base pressure in the tunnel-installed model exhibits increased deviations in the azimuthal location of up to 7.5%. Still, the equivalent unconstrained flow compares reasonably well and falls within the observed range of pressure distribution, while the corresponding deviation on the cavity wall is less than 1%. This demonstrates that local base flow similarity can be established and quantified with respect to unconstrained flow conditions. This is of high practical importance, owing to the size of most closed transonic wind tunnels found in academia, and allows for base flow and base drag reduction analyses, which are typically based on surface pressure measurements, to be performed even under high blockage ratios.

Acknowledgments

The authors would like to express their gratitude to Reaction Engines Ltd., Rolls-Royce Plc., and the Cranfield Air and Space Propulsion Institute (CASPI) for funding this project and granting permission to publish this research.

References

[1] Varvill, R., and Bond, A., "A comparison of propulsion concepts for SSTO reusable launchers," *Journal of the British Interplanetary Society*, Vol. 56, 2003, pp. 108–117.

[2] McClinton, C. R., "High speed/hypersonic aircraft propulsion technology development," *Advances on propulsion technology for high-speed aircraft. Educational Notes RTO-EN-AVT-150*, Vol. 1, NATO RTO, Neuilly-sur-Seine, France, 2007, pp. 1–32.

[3] Ingenito, A., *Subsonic Combustion Ramjet Design*, Springer Nature, Switcherland, 2021. https://doi.org//10.1007/978-3-030-66881-5.

[4] Murthy, S., and Curran, E., *Scramjet Propulsion*, AIAA, 2001. https://doi.org/10.2514/4.866609.

[5] Bogar, T., Eiswirth, E., Couch, L., Hunt, J., and McClinton, C., "Conceptual design of a Mach 10, global reach reconnaissance aircraft," *32nd Joint Propulsion Conference and Exhibition*, 1996. https://doi.org/10.2514/6.1996-2894.

[6] Daines, R., and Segal, C., "Combined Rocket and Airbreathing Propulsion Systems for Space-Launch Applications," *Journal of Propulsion and Power*, Vol. 14, No. 5, 2012, pp. 605–612. https://doi.org/10.2514/2.5352.

[7] Jian, D., and Qiuru, Z., "Key technologies for thermodynamic cycle of precooled engines: A review," *Acta Astronautica*, Vol. 177, 2020, pp. 299–312. https://doi.org/10.1016/j.actaastro.2020.07.039.

[8] Tsentis, S., Gkoutzamanis, V., Gaitanis, A., and Kalfas, I., "Multi-platform App-embedded Model for Hybrid Air-Breathing Rocket-Cycle Engine in Hypersonic Atmospheric Ascent," *The Aeronautical Journal*, Vol. 125 (1291), 2021, pp. 1631–1653. https://doi.org/10.1017/aer.2021.3.

[9] Villace, V. F., and Paniagua, G., "Simulation of a Combined Cycle for High Speed Propulsion," *48th AIAA Aerospace Sciences Meeting Including the New Horizons Forum and Aerospace Exposition*, Orlando, Florida, 2010. https://doi.org/10.2514/6.2010-1125.

[10] Mariotti, A., and Buresti, G., "Experimental investigation on the influence of boundary layer thickness on the base pressure and near-wake flow features of an axisymmetric blunt-based body," *Exp Fluids*, Vol. 54, No. 1612, 2013. https://doi.org/10.1007/s00348-013-1612-5.

[11] Mariotti, A., Buresti, G., and Salvetti, M. V., "Connection between base drag, separating boundary layer characteristics and wake mean recirculation length of an axisymmetric blunt-based body," *Journal of Fluids and Structures*, Vol. 55, 2015, pp. 191–203. https://doi.org/10.1016/j.jfluidstructs.2015.02.012.

[12] Tran, T., Dinh, H., and Chu, H. e. a., "Effect of boattail angle on near-wake flow and drag of axisymmetric models: a numerical approach," *J Mech Sci Technol*, Vol. 35, 2021, pp. 563–573. https://doi.org/10.1007/s12206-021-0115-1.

[13] Deprés, D., Reijasse, P., and Dussauge, J. P., "Analysis of Unsteadiness in Afterbody Transonic Flows," *AIAA Journal*, Vol. 42, No. 12, 2004, pp. 2541–2550. https://doi.org/10.2514/1.7000.

[14] Paciorri, R., Sabetta, F., Valenza, F., Fauci, R., Passaro, A., and Baccarella, D., "Base-Pressure Experimental Investigation on a Space Launcher in Subsonic Regime," *Journal of Spacecraft and Rockets*, Vol. 50, No. 3, 2013, pp. 572–578. https://doi.org/10.2514/1.A32283.

[15] Scharnowski, S., and Kähler, C., "Investigation of the base flow of a generic space launcher with dual-bell nozzle," *CEAS Space Journal*, Vol. 13, 2021, pp. 197–216. https://doi.org/10.1007/s12567-020-00333-5.

[16] Saile, D., Kühl, V., and Gülhan, A., "On the subsonic near-wake of a space launcher configuration with exhaust jet," *Experiments in Fluids*, Vol. 60, No. 165, 2019. https://doi.org/10.1007/s00348-019-2801-7.

[17] Schwane, R., "Numerical Prediction and Experimental Validation of Unsteady Loads on ARIANE5 and VEGA," *Journal of Spacecraft and Rockets*, Vol. 52, No. 1, 2015, pp. 54–62. https://doi.org/10.2514/1.A32793.

[18] Saile, D., Kühl, V., and Gülhan, A., "On subsonic near-wake flows of a space launcher configuration with various base geometries," *Experiments in Fluids*, Vol. 62, No. 122, 2021. https://doi.org/10.1007/s00348-021-03149-z.

[19] Statnikov, V., Sayadi, T., Meinke, M., Schmid, P., and Schröder, W., "Analysis of pressure perturbation sources on a generic space launcher after-body in supersonic flow using zonal turbulence modeling and dynamic mode decomposition," *Physics of Fluids*, Vol. 27, No. 016103, 2015. https://doi.org/10.1063/1.4906219.

[20] Hammond, W. E., *Design Methodologies for Space Transportation Systems*, AIAA, Virginia, 2001. https://doi.org/10.2514/4.861734.

[21] Meliga, P., and Reijasse, P., "Unsteady Transonic Flow Behind An Axisymmetric Afterbody Equipped With Two Boosters," *25th AIAA Applied Aerodynamics Conference*, 2012. https://doi.org/10.2514/6.2007-4564.

[22] Morel, T., "Effect of Base Cavities on the Aerodynamic Drag of an Axisymmetric Cylinder," *Aeronautical Quarterly*, Vol. 30, 1990, pp. 400–412. https://doi.org/10.1017/s0001925900008611.

[23] Tripathi, A., Manisankar, C., and Verma, S. B., "Control of base pressure for a boat-tailed axisymmetric afterbody via base geometry modifications," *Aerospace Science and Technology*, Vol. 45, 2015, pp. 284–293. https://doi.org/10.1016/j.ast.2015.05.021.

[24] Viswanath, P. R., and Patil, S. R., "Effectiveness of passive devices for axisymmetric base drag reduction at Mach 2," *Journal of Spacecraft and Rockets*, Vol. 27, No. 3, 1990, pp. 234–237. https://doi.org/10.2514/3.26130.

[25] Viswanath, P. R., "Flow Management Techniques for Base and Afterbody Drag Reduction," *Progress in Aerospace Sciences*, Vol. 32, 1996, pp. 79–129.

[26] Tanner, M., "Reduction of Base Drag," *Progress in Aerospace Sciences*, Vol. 16, No. 4, 1975, pp. 369–384.

[27] Tsentis, S., Goulos, I., Prince, S., Pachidis, V., and Zmijanovic, V., "Propulsion Aerodynamics for a Novel High-Speed Exhaust System," *Journal of Engineering for Gas Turbines and Power*, 2023, pp. 1–33. https://doi.org/10.1115/1.4063416.

[28] Roncioni, P., Vitagliano, P., Gregorio, F., Pezzella, G., Romano, L., and Paglia, F., "Aerodynamic Appraisal of the VEGA-C Launcher," *Journal of Spacecraft and Rockets*, Vol. 0, No. 0, 0, pp. 1–15. https://doi.org/10.2514/1.A35610.

[29] Greenwell, D., "Transonic industrial wind tunnel testing in the 2020s," *The Aeronautical Journal*, Vol. 126, No. 1295, 2022, p. 125–151. https://doi.org/10.1017/aer.2021.107.

[30] Chanetz, B., Délery, J., Gilliéron, P., Gnemmi, P., Gowree, E. R., and Perrier, P., *Experimental Aerodynamics: An Introductory Guide*, Springer, 2020. https://doi.org/10.1007/978-3-030-35562-3.

[31] Goethert, B. H., "Transonic Wind Tunnel Testing," AGARDograph No. 49, Advisory Group for Aerospace Research and Development, 1961.

[32] Marschner, B., "The Flow Over a Body in a Choked Wind Tunnel and in a Sonic Free Jet," *Journal of the Aeronautical Sciences*, Vol. 23, No. 4, 1956, pp. 368–376. https://doi.org/10.2514/8.3567.

[33] MIDAP, S. G., "Subsonic Wind Tunnel Wall Corrections," AGARDograph No. 109, Advisory Group for Aerospace Research and Development, 7 Rue Ancelle 92200 Neuilly, Sur Seine, France, 1966.

[34] MIDAP, S. G., "Wind Tunnel Wall Correction," AGARDograph No. 336, Advisory Group for Aerospace Research and Development, 7 Rue Ancelle 92200 Neuilly, Sur Seine, France, 1998.

[35] Zucrow, M. J., and Hoffman, J. D., *Gas Dynamics*, John Wiley and Sons, New York, 1976.

[36] Sauer, R., "General Characteristics of the Flow through Nozzles at Near Critical Speeds," Memorandum No.1147, NACA, Washington, DC, 1947.

[37] MIDAP, S. G., "Guide to In-Flight Thrust Measurement of Turbojets and Fan Engines," AGARDograph No. 237, Advisory Group for Aerospace Research and Development, 7 Rue Ancelle 92200 Neuilly, Sur Seine, France, 1979.

[38] *Ansys FLUENT Meshing User Guide*, Ansys Inc., 275 Technology Drive, Canonsbug, PA 15317, 2012.

[39] Zhou, C., and Chen, M., "Aerodynamic Simulation of Helicopter Based on Polyhedron Nested Grid Technology," *Applied Sciences*, Vol. 10, No. 22:8304, 2020. https://doi.org/10.3390/app10228304.

[40] Wang, W., Cao, Y., and Okaze, T., "Comparison of hexahedral, tetrahedral and polyhedral cells for reproducing the wind field around an isolated building by LES," *Building and Environment*, Vol. 195, No. 107717, 2021. https://doi.org/https://doi.org/10.1016/j.buildenv.2021.107717.

[41] Richardson, L. F., and Gaunt, J. A., "The Deferred Approach to the Limit," *Philos. Trans. R. Soc. London*, Vol. Ser. A, 226, 1927, pp. 307–357.

[42] Celik, I. B., Ghia, U., Roache, P. J., Freitas, C. J., Coleman, H., and Raad, P. E., "Procedure for Estimation and Reporting of Uncertainty Due to Discretization in CFD Applications," *Journal of Fluids Engineering*, Vol. 130, No. 7, 2008. https://doi.org/10.1115/1.2960953.

[43] *Ansys Fluent Theory Guide*, Ansys Inc., 275 Technology Drive, Canonsbug, PA 15317, 2013.

[44] Menter, F. R., "Two-equation eddy-viscosity turbulence models for engineering applications," *AIAA Journal*, Vol. 32, 1994, pp. 1598–1065. https://doi.org/10.2514/3.12149.

[45] Allamaprabhu, C., Raghunandan, B., and Morinigo, J., *Improved Prediction of Flow Separation in Thrust Optimized Parabolic Nozzles with FLUENT*, 2011. https://doi.org/10.2514/6.2011-5689.

[46] Hasan, R. G. M., McGuirk, J. J., Apsley, D. D., and Leschziner, M. A., "A turbulence model study of separated 3D jet/afterbody flow," *The Aeronautical Journal*, Vol. 108, No. 1079, 2004, p. 1–14. https://doi.org/10.1017/S0001924000004942.

[47] Roe, P. L., "Approximate Riemann solvers, parameter vectors, and difference schemes," *Journal of Computational Physics*, Vol. 43, No. 2, 1981, pp. 357–372. https://doi.org/10.1016/0021-9991(81)90128-5.

[48] Walsh, P., and Fletcher, P., *Gas Turbine Performance*, Blackwell Publishing, 2004.

[49] Sutherland, W., "The viscosity of gases and molecular forces," *Philos. Mag.*, Vol. 36, 1893, pp. 507–531.

[50] *Ansys Workbench User's Guide*, Ansys Inc., 275 Technology Drive, Canonsbug, PA 15317, 2009.

Wind tunnel installation effects on the base flow for a high-speed exhaust system

Tsentis, Spyros

2024-01-04

Tsentis S, Goulos I, Prince S, et al., (2024) Wind tunnel installation effects on the base flow for a high-speed exhaust system. In: AIAA SCITECH 2024 Forum, 8-12 January 2024, Orlando, Florida, Paper number AIAA 2024-1774

https://doi.org/10.2514/6.2024-1774